

# Next-to-leading order predictions for $WW$ +jet production

John M. Campbell

*Fermilab, PO Box 500, Batavia, IL 60510, USA*

David J. Miller

*School of Physics and Astronomy, University of Glasgow, Glasgow, G12 8QQ, UK*

Tania Robens

*IKTP, Technische Universität Dresden,  
Zellescher Weg 19, D-01069, Dresden, Germany*

(Dated: October 10, 2018)

In this work we report on a next-to-leading order calculation of  $WW$  + jet production at hadron colliders, with subsequent leptonic decays of the  $W$ -bosons included. The calculation of the one-loop contributions is performed using generalized unitarity methods in order to derive analytic expressions for the relevant amplitudes. These amplitudes have been implemented in the parton-level Monte Carlo generator MCFM, which we use to provide a complete next-to-leading order calculation. Predictions for total cross-sections, as well as differential distributions for several key observables, are computed both for the LHC operating at 14 TeV as well as for a possible future 100 TeV proton-proton collider.

## 1. INTRODUCTION

In this paper we report on a calculation of the next-to-leading order (NLO) QCD corrections to the process of  $W$  pair production in association with a jet using unitarity methods, taking into account spin correlations in the leptonic decays of the  $W$  bosons. This process is important for a number of reasons. Firstly, the rate for  $WW$  production at the LHC is significant and thus the  $WW$  process (and more generally all the vector boson pair production processes) provide a useful laboratory with which to probe the Standard Model (SM). Indeed, already in Run I of the LHC, the ATLAS and CMS experiments have been able to investigate the properties of the  $WW$  process in some detail [1–9]. The presence of an additional jet in the detector acceptance only slightly reduces the cross-section, by around a factor of 2–3 for typical jet cuts. In addition, this process also represents an important background to the production of a Higgs boson with subsequent decay into  $W$  pairs, either through the gluon-fusion channel with an additional jet present, or through weak boson fusion where only one of the forward jets is detected. Analyses of  $WW$  events also provide strong constraints on anomalous triple and quartic gauge couplings [1, 6, 7, 10] and represent important backgrounds for searches for additional scalars of higher mass [11, 12].

Aside from the immediate relevance to the LHC experimental program, the one-loop amplitudes for the process at hand represent an important component of the NNLO corrections to the  $WW$  process. Indeed, calculations of the corresponding two-loop amplitudes [13–18] have already allowed first determinations of the NNLO contribution [15]. In such a calculation the one-loop  $WW$  + 3 parton amplitudes must be evaluated in the limit in which the gluon is soft, or the quark and antiquark are collinear. This is true for both the sector-decomposition and antenna-subtraction methods that have mostly been employed in NNLO calculations thus far and also for the recently-introduced SCET-based  $N$ -jettiness method [19, 20]. For this reason it is important that the form of the amplitudes be both numerically stable and efficiently evaluated.



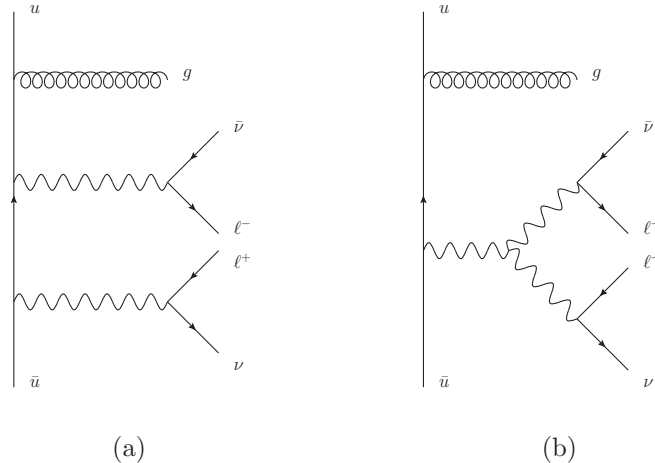


FIG. 1: Sample diagrams entering the calculation of the leading order amplitude for the  $WW$ +jet process, corresponding to (a)  $W$  emission from the quark line and (b) emission from an intermediate  $Z$  boson or photon.

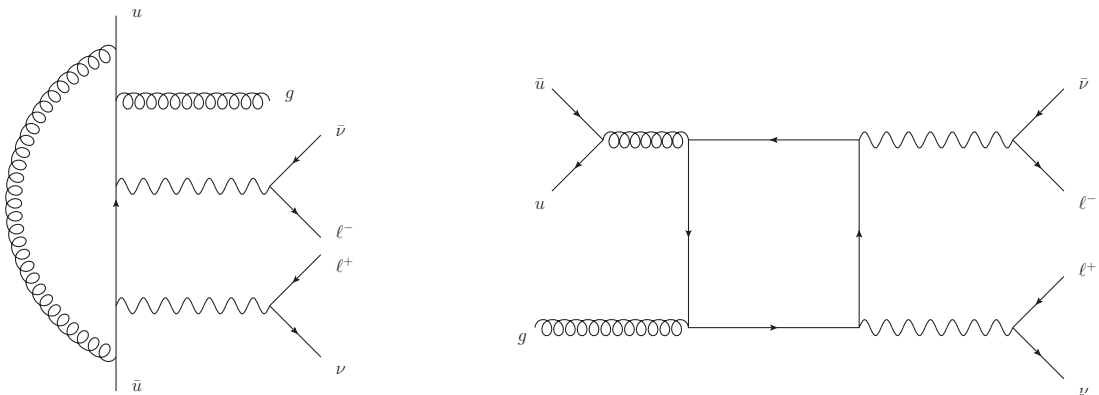


FIG. 2: Sample diagrams entering the calculation of the one-loop amplitude for the  $WW$ +jet process. The one-loop diagrams can be categorized according to whether a gluon dresses a leading-order amplitude (left), or whether the diagram includes a closed fermion loop (right).

amplitude is decomposed in terms of the usual one-loop basis of box, triangle and bubble integrals, i.e.

$$\mathcal{A}(\{p_i\}) = \sum_j d_j I_4^j + \sum_j c_j I_3^j + \sum_j b_j I_2^j + R. \quad (2)$$

In this equation  $I_n^j$  represents a scalar loop integral with  $n$  propagators, commonly referred to as box ( $n = 4$ ), triangle ( $n = 3$ ) and bubble ( $n = 2$ ) integrals. The integral coefficients  $d_j$ ,  $c_j$  and  $b_j$  can be obtained by the application of unitarity cuts in four dimensions [21–25]. The rational remainder term  $R$  can be determined using similar cutting rules, after the inclusion of a fictitious mass for the particles propagating in the loop [26]. Since the tree-level on-shell amplitudes that appear in the cutting procedure are quite complex, this procedure has been performed using the help of the S@M Mathematica package [49]. The evaluation of the scalar integrals appearing in Eq. (2) has been performed with the aid of the QCDDLoop Fortran library [50].

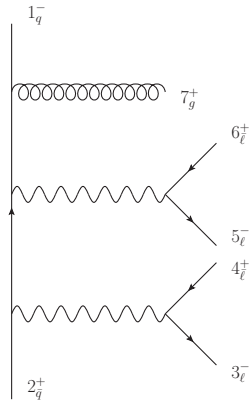


FIG. 3: The notation used in the calculation of the  $WW$ +jet process, corresponding to Eq. (3).

## 2.1. Details

In this section we will present a number of the integral coefficients that were computed using the unitarity techniques described previously. For the sake of brevity we will show coefficients that do not involve lengthy algebraic manipulation and are therefore particularly compact. The remaining coefficients can be inspected in the distributed MCFM code.

In order to establish the notation for these coefficients we first discuss the corresponding leading-order results. We consider all particles outgoing and consider the process,

$$0 \rightarrow q^-(p_1) + \bar{q}^+(p_2) + \ell^-(p_3) + \bar{\ell}^+(p_4) + \ell^-(p_5) + \bar{\ell}^+(p_6) + g^+(p_7), \quad (3)$$

also shown in Figure 3, where momentum assignments are shown in parentheses and superscripts denote the particle helicities and polarizations. This is the basic configuration for which we compute all amplitudes; other helicity configurations are obtained by means of charge conjugation and parity relations. Tree-level amplitudes for this process have been presented in detail in Refs. [38, 46], whose notation we follow closely. The full amplitude can be written in terms of two primitive amplitudes,  $A^{(a)}$  and  $A^{(b)}$  corresponding to diagrams of the two types depicted in Figure 1. The full amplitude is obtained from the primitive ones by dressing with appropriate color and coupling factors [46]. The explicit forms, for the assignment of momenta shown in Eq. (3), are:

$$\begin{aligned} A^{(a)}(1_q^-, 2_{\bar{q}}^+, 3_l^-, 4_l^+, 5_l^-, 6_l^+, 7_g^+) \\ = \frac{1}{s_{34} - m_W^2} \frac{1}{s_{56} - m_W^2} \frac{1}{s_{156}} \frac{\langle 15 \rangle}{\langle 17 \rangle} \left\{ \frac{[6|1 + 5|3][4|2 + 7|1]}{\langle 27 \rangle} + \frac{[65]\langle 51 \rangle [7|2 + 4|3][42]}{s_{234}} \right\}, \\ A^{(b)}(1_q^-, 2_{\bar{q}}^+, 3_l^-, 4_l^+, 5_l^-, 6_l^+, 7_g^+) = \frac{1}{s_{34} - m_W^2} \frac{1}{s_{56} - m_W^2} \frac{1}{s_{127}} \frac{1}{\langle 17 \rangle \langle 27 \rangle} \times \\ \left\{ \langle 15 \rangle \langle 1|2 + 7|6 \rangle \langle 3|5 + 6|4 \rangle - \langle 13 \rangle \langle 1|2 + 7|4 \rangle \langle 5|3 + 4|6 \rangle - \langle 35 \rangle [46] \langle 1|(3 + 4)(2 + 7)|1 \rangle \right\}. \end{aligned}$$

The coefficients discussed below all appear in the amplitude representing the diagrams of Figure 2 (left), i.e. they do not contain a closed loop of fermions. The decomposition of the amplitude into the form shown in Eq. (2) contains five basis integrals corresponding to “three-mass” boxes, i.e. four-point integrals with three non-lightlike external legs. This naturally leads to a plethora of three-mass triangles, whose coefficients do not lend themselves easily to a compact representation

in terms of straightforward spinor products. As a result, many of the coefficients are considerably more complex than those presented here. To simplify the calculation slightly, we use the known singular structure of the amplitude to determine one of the bubble coefficients from the remainder.

As a representative box integral coefficient we choose the one corresponding to the basis integral  $I_4(s_{56}, s_{34}, 0, s_{17}; s_{127}, s_{234})$ . We here show the leading color integral coefficient, which receives a pre-factor of  $N_c$ . It can be written as,

$$d(s_{56}, s_{34}, 0, s_{17}; s_{127}, s_{234}) = \frac{1}{s_{34} - m_W^2} \frac{1}{s_{56} - m_W^2} \frac{\langle 12 \rangle^2 \langle 2|P|2 \rangle}{2 \langle 27 \rangle \langle 17 \rangle} \times \\ \left( [42] - \frac{\langle 2|P|4 \rangle}{D} \right) \left( \langle 3|2 + 4|6 \rangle - \frac{\langle 23 \rangle \langle 2|P|6 \rangle}{D} \right) \left( \frac{[71] \langle 15 \rangle}{\langle 2|P|7 \rangle} + \frac{\langle 25 \rangle}{D} \right) \quad (4)$$

where the compound momentum  $P$  and denominator factor  $D$  are defined by,

$$P = s_{17} p_{34} + s_{234} p_{17}, \quad D = \langle 2|(3+4)(1+7)|2 \rangle. \quad (5)$$

The factors of  $D$  can be put into a more familiar form by relating them to the product  $DD^*$ , where the complex conjugate of  $D$  is simply given by  $D^* = [2|(3+4)(1+7)|2]$ . The product can be written as a trace of gamma matrices that evaluates to,

$$DD^* = 4s_{34}(p_2 \cdot p_{17})^2 + 4s_{17}(p_2 \cdot p_{34})^2 - 8(p_2 \cdot p_{17})(p_2 \cdot p_{34})(p_{17} \cdot p_{34}). \quad (6)$$

This is just the Gram determinant for this basis integral; its presence, when raised to a sufficiently high power, can lead to numerical instability in phase space regions where it is very small. To avoid any such issues we veto phase regions where cancellations between the terms in Eq. (6) (and equivalent expressions for the other box integrals) occur at the level of  $10^{-6}$  or more. In our studies this occurs only very rarely, in about one in a million events, so that the effects of such a veto are tiny compared to the anticipated level of precision.

For the calculation of the integral coefficients in four dimensions, the only triangle coefficients that must be computed correspond to integrals with three massive external legs. Triangle integrals with one or more lightlike legs only contribute to the overall pole structure, which is known a priori. The three mass triangle coefficients are most easily expressed in terms of an extended set of momenta that naturally appear in the unitarity approach [24]. For example, the coefficient of the (leading-colour) basis integral  $I_3(s_{34}, s_{27}, s_{156})$  is,

$$c(s_{34}, s_{27}, s_{156}) = \frac{1}{2} \frac{1}{s_{34} - m_W^2} \frac{1}{s_{56} - m_W^2} \sum_{\gamma=\gamma_{1,2}} \frac{s_{27} [4K_2^b] [72] [65] \langle K_1^b 2 \rangle \langle K_1^b 3 \rangle \langle 15 \rangle^2}{(\gamma - s_{27}) [7K_2^b] \langle K_1^b 1 \rangle \langle K_1^b 7 \rangle \langle 27 \rangle} \quad (7)$$

where the additional momenta  $K_1^b$  and  $K_2^b$  are defined by,

$$K_1^b = \frac{\gamma [\gamma p_{27} + s_{27} p_{34}]}{\gamma^2 - s_{27} s_{34}}, \quad K_2^b = -\frac{\gamma [\gamma p_{34} + s_{34} p_{27}]}{\gamma^2 - s_{27} s_{34}}. \quad (8)$$

The values of  $\gamma$  appearing in these equations are determined by the condition that  $K_1^b$  and  $K_2^b$  are lightlike,

$$\gamma_{1,2} = p_{27} \cdot p_{34} \pm \sqrt{(p_{27} \cdot p_{34})^2 - s_{27} s_{34}}. \quad (9)$$

The expressions for the bubble coefficients are, in general, rather complicated due to the complexity of the tree amplitudes that appear either side of the cut. However, the coefficient of the

calculation	parameters	$\sigma^{\text{NLO}}$ [pb]
MCFM	default	14.571 (18)
MG5	default	14.547 (19)
MG5	$m_h \times 10, m_t \times 10$	14.615 (21)
MG5	$m_h \times 100, m_t \times 100$	14.563 (19)
DKU [39]	default	14.678 (10)

TABLE I: Total NLO cross-sections for the process  $pp \rightarrow W^+ W^- j$  at the 14 TeV LHC, with parameter specifications as in Ref. [52] (“default”), except where noted otherwise.

bubble integral  $I_2$  ( $s_{156}$ ), that appears at leading colour, is rather simple. It is given by,

$$\begin{aligned}
b(s_{156}) = & \frac{1}{s_{34} - m_W^2} \frac{1}{s_{56} - m_W^2} \frac{\langle 56 \rangle [43]}{\langle 27 \rangle \langle 7|P|1 \rangle} \times \left\{ - \frac{\langle 15 \rangle [56] \langle 3|P|1 \rangle^2}{s_{156} \langle 1|P|1 \rangle} \left[ \frac{\langle 15 \rangle [56]}{2 \langle 1|P|1 \rangle} + \frac{\langle 7|P|6 \rangle}{\langle 7|P|1 \rangle} \right] \right. \\
& \left. + \frac{\langle 73 \rangle^2 \langle 7|P|6 \rangle [76]}{\langle 7|P|7 \rangle} \left[ \frac{1}{\langle 7|P|7 \rangle} \left( \frac{\langle 3|P|7 \rangle}{\langle 37 \rangle} + \frac{[76] s_{156}}{2 \langle 7|P|6 \rangle} \right) + \frac{\langle 3|P|1 \rangle}{\langle 37 \rangle \langle 7|P|1 \rangle} \right] \right\}, \quad (10)
\end{aligned}$$

where the momentum across the cut is  $P = p_1 + p_5 + p_6$ .

## 2.2. Validation

In order to verify the correctness of our calculation we have performed a variety of cross-checks on both the one-loop amplitudes and the complete NLO calculation. These consist of both independent calculations by other methods as well as comparisons with results previously reported in the literature.

For the one-loop amplitude it is useful to perform cross-checks of the calculation at single points in phase space. All amplitudes have been cross-checked with an independent numerical implementation of  $D$ -dimensional unitarity based on ref. [51], which allows a verification of individual basis integral coefficients. We find agreement with both the results presented in Table 3 (Appendix B) of Ref. [38] and those of Table 8 (Section 12.4) of Ref. [52] for the case of non-decaying  $W$ -bosons.

To make a direct comparison at the level of the complete NLO cross-section, we have performed a calculation in the set-up of Ref. [52] using aMC@NLO/Madgraph 5 [53, 54]. We find complete agreement between our result and Madgraph5, with integration errors for both being at the per mille level, as shown in Table I. The calculations of Ref. [38, 52] also include contributions from top and bottom quarks for diagrams with internal quark loops, as well as Higgs-induced diagrams for Ref. [52]. In order to assess the effect of the loop of third generation quarks, and the Higgs boson, we have artificially inflated the top quark and Higgs boson masses in order to marginalize their effects on the NLO cross-section. Variations of the total cross-section are within the respective integration error, cf. Table I. Therefore, although these contributions are not included in our calculation, they do not have a significant effect at this level. We find a small difference, of about 0.75%, with the calculation of Ref. [52], as reported in Table I. We find larger differences with the published results of Ref. [38], at the level of a few percent. Given the excellent agreement with the other available results, we ascribe this to under-estimated Monte Carlo uncertainty in the earlier calculation.

$m_W$	80.385 GeV	$\Gamma_W$	2.085 GeV
$m_Z$	91.1876 GeV	$\Gamma_Z$	2.4952 GeV
$e^2$	0.095032	$g_W^2$	0.42635
$\sin^2 \theta_W$	0.22290	$G_F$	$0.116638 \times 10^{-4}$

TABLE II: The values of the mass, width and electroweak parameters used to produce the results in this paper.

### 3. PHENOMENOLOGY

The results presented in this section have been obtained using the parameters shown in Table II. Note that we do not include the effects of any third-generation quarks, either as external particles or in internal loops. Since the effects of a non-diagonal CKM matrix are very small, we also do not include them here. In calculations of LO quantities we employ the CTEQ6L1 PDF set [55], while at NLO we use CT10 [56]. The renormalization and factorization scales are usually chosen to be the same,  $\mu_R = \mu_F = \mu$ , with our default scale choice  $\mu = \mu_0$  given by,

$$\mu_0 \equiv \frac{H_T}{2} = \frac{1}{2} \sum_i p_{\perp}^i . \quad (11)$$

The sum over the index  $i$  runs over all final state leptons and partons. This choice of scale captures some of the dynamics of the process in a way that is missed in, for instance, a fixed scale choice  $\mu = m_W$  or other common event-by-event scales [57]. Jets are defined using the anti- $k_T$  algorithm with separation parameter  $R = 0.5$  and must satisfy,

$$p_{\perp}^{\text{jet}} > 25 \text{ GeV} , \quad |\eta^{\text{jet}}| < 4.5 . \quad (12)$$

Since many phenomenological studies of this process have already been performed, both at NLO [38–41] and including the effects of a parton shower at NLO [42], in this paper we restrict ourselves to a small number of pertinent applications. To this end we consider the immediate prospects in Run 2 of the LHC by presenting cross-sections at 14 TeV under a range of possible experimental cuts. For a longer-term view, we also consider the situation at a possible Future Circular Collider with proton-proton collisions at 100 TeV.

The total cross-sections for  $WW$ +jet production at these colliders are collated in Table III. The effect of the decays of the  $W$  bosons are not included and the jet is defined using the cuts given in Eq. (12). The theoretical uncertainty is computed by using a series of scale variations about the central choice  $\mu_0$ . In order to properly explore this uncertainty, we decouple  $\mu_R$  and  $\mu_F$  and consider their variation separately. The uncertainty corresponds to the most extreme predictions for the four choices,

$$\{\mu_R, \mu_F\} = \{2\mu_0, 2\mu_0\} , \{\mu_0/2, \mu_0/2\} , \{2\mu_0, \mu_0/2\} , \{\mu_0/2, 2\mu_0\} . \quad (13)$$

At the LHC the uncertainty estimate corresponds to the first two variations in Eq. (13), i.e. when the scales are varied together. At 100 TeV the last two scale variations are most important, due to an accidental cancellation between the dependence on factorization and renormalization scales when they are varied together in the same direction. At the LHC this estimate of the uncertainty decreases from approximately 10% at LO to about 4% at NLO. At 100 TeV the estimates of the uncertainty, both at LO and NLO, are approximately a factor of two larger. For reference, the corresponding NLO cross-sections for inclusive  $WW$  production with the same input parameters are approximately 120pb at 14 TeV and 1300pb at 100 TeV.

$\sqrt{s}$	$\sigma_{LO}$ [pb]	$\sigma_{NLO}$ [pb]
13 TeV	$34.9^{+11.4\%}_{-11.0\%}$	$42.9^{+3.7\%}_{-3.7\%}$
14 TeV	$39.5^{+11.7\%}_{-11.0\%}$	$48.6^{+3.8\%}_{-4.0\%}$
100 TeV	$648^{+22.3\%}_{-23.8\%}$	$740^{+4.5\%}_{-9.3\%}$

TABLE III: Cross-sections for the process  $pp \rightarrow WW+\text{jet}$  at proton-proton colliders of various energies, together with estimates of the theoretical uncertainty from scale variation according to Eq. (13). Monte Carlo uncertainties are at most a single unit in the last digit shown in the table.

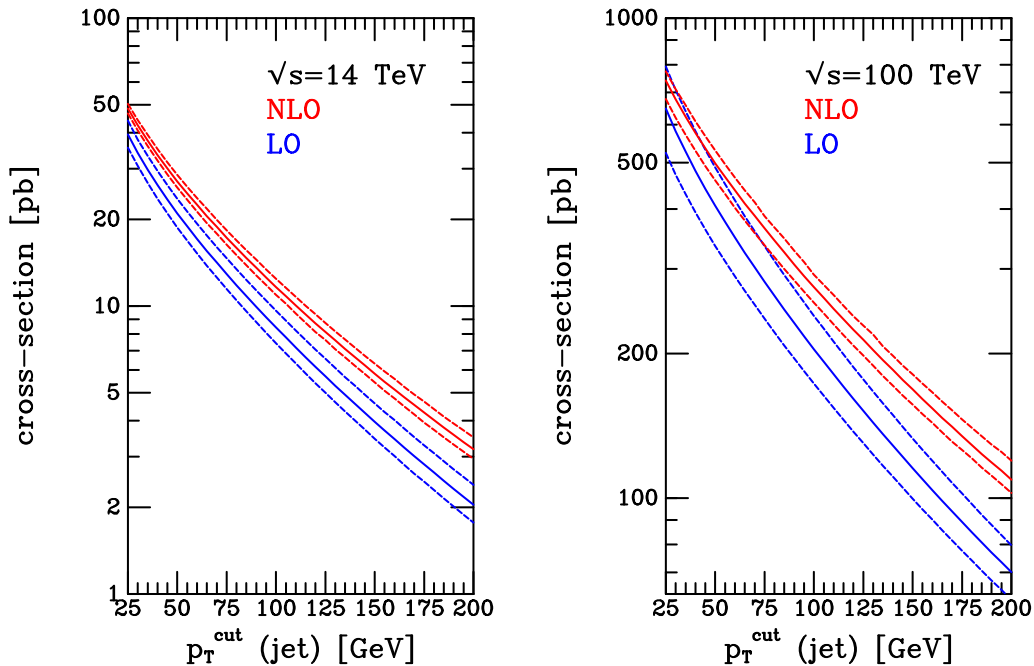


FIG. 4: Cross-sections at  $\sqrt{s} = 14$  TeV (left) and 100 TeV (right), as a function of the transverse momentum cut on the jet. The prediction at each order is shown as a solid line, with the dotted lines indicating the scale uncertainty corresponding to a factor of two variation about the central scale.

To assess the effect of jet cuts at higher transverse momenta, we also present the cross-sections at LO and NLO as a function of the minimum jet  $p_{\perp}$  in Figure 4. The size of the higher-order correction increases with the minimum jet  $p_{\perp}$ , although the relative uncertainty is approximately the same. We note that the relative importance of the  $WW+\text{jet}$  final state, compared to inclusive  $WW$  production, is greater at the 100 TeV collider.

We now turn away from more inclusive quantities and instead focus on particular sets of cuts targeted at specific analyses. We first consider the case of 14 TeV LHC running, with a set of cuts inspired by the ATLAS determination of the spin and parity of the Higgs boson presented in Ref. [58]. The  $WW$  process constitutes the largest irreducible background in the  $H \rightarrow WW^*$  decay channel and a cocktail of cuts must be applied in order to access information about the Higgs boson. Our analysis is limited to the consideration of the dominant  $WW+\text{jet}$  background and somewhat simplified with respect to the experimental one. The cuts that we apply are summarized in Table IV. These include constraints on the transverse mass of  $(X, E_T^{\text{miss}})$  systems,  $m_T^X$ , where

variable	cut
$p_{\perp,j}$	$> 25$ GeV
$ \eta_j $	$< 4.5$
$ \eta_\ell $	$< 2.5$
$p_{\perp,\ell_1}$	$> 22$ GeV
$p_{\perp,\ell_2}$	$> 15$ GeV
$m_{\ell\ell}$	$\in [10, 80]$ GeV
$p_{\perp}^{\text{miss}}$	$> 20$ GeV
$\Delta\Phi_{\ell\ell}$	$< 2.8$
$m_T^{\ell\ell}$	$< 150$ GeV
$\max[m_T^{\ell_1}, m_T^{\ell_2}]$	$> 50$ GeV

TABLE IV: Cuts applied in the 14 TeV analysis, corresponding to the “full” set of cuts. The jet cuts, corresponding to the first two lines in the table, are the only ones applied for the “basic” cross-section.

cuts	$\sigma^{\text{LO}}$ [fb]	$\sigma^{\text{NLO}}$ [fb]	$K$
basic	462.0(2)	568.4(2)	1.23
full	67.12(4)	83.91(5)	1.25
spin-2	58.21(4)	71.32(5)	1.23

TABLE V: Cross-sections at 14 TeV, for the cuts specified in Table IV (basic, full) and also in Eq. (15) (spin-2). Monte Carlo uncertainties are indicated in parentheses and are smaller than the per mille level.

$X \in (\ell\ell, \ell_1, \ell_2)$ , with  $p_{\ell\ell} = p_{\ell_1} + p_{\ell_2}$ . This quantity is defined by<sup>1</sup>,

$$m_T^X = \sqrt{2 p_{\perp}^X E_T^{\text{miss}} \left( 1 - \cos \Delta\Phi(\vec{p}_T^X, \vec{E}_T^{\text{miss}}) \right)}. \quad (14)$$

In the results that follow we shall always consider the decay of each  $W$  boson into a single lepton family, i.e. the Born level quark-antiquark process we consider is the one shown in Eq. (1). The cross-sections under these cuts are given in Table V. In order to assess their effect, we also show for comparison the cross sections obtained using only the jet cuts, i.e. the top two lines of the cuts in Table IV. In addition, we consider the imposition of an additional constraint on the transverse momentum of the putative Higgs boson,

$$p_{\perp}^H \equiv \sum p_{T,\text{miss}} + p_{T,\ell\ell} < 125 \text{ GeV}. \quad (15)$$

Such a cut is useful when testing the spin-2 hypothesis for the Higgs boson [58]. The table also shows the  $K$ -factor, defined by  $K = \sigma^{\text{NLO}}/\sigma^{\text{LO}}$ , which we find is rather insensitive to which set of cuts is applied.

Going beyond the pure cross-section calculation, it is interesting to examine the effect of NLO corrections on a few key differential distributions. We shall consider a number that have already entered in the discussion of the cuts –  $m_T^{\ell\ell}$ ,  $\Delta\Phi_{\ell\ell}$  and  $m_{\ell\ell}$  – as well as the transverse momentum of the lead jet,  $p_{\perp}^{j_1}$ . These quantities are shown in Figure 5 where, for comparison, the LO prediction has been rescaled by the  $K$ -factor from Table V. This indicates that there is very little difference

<sup>1</sup> See, for instance, Eq. (3) of Ref. [11].

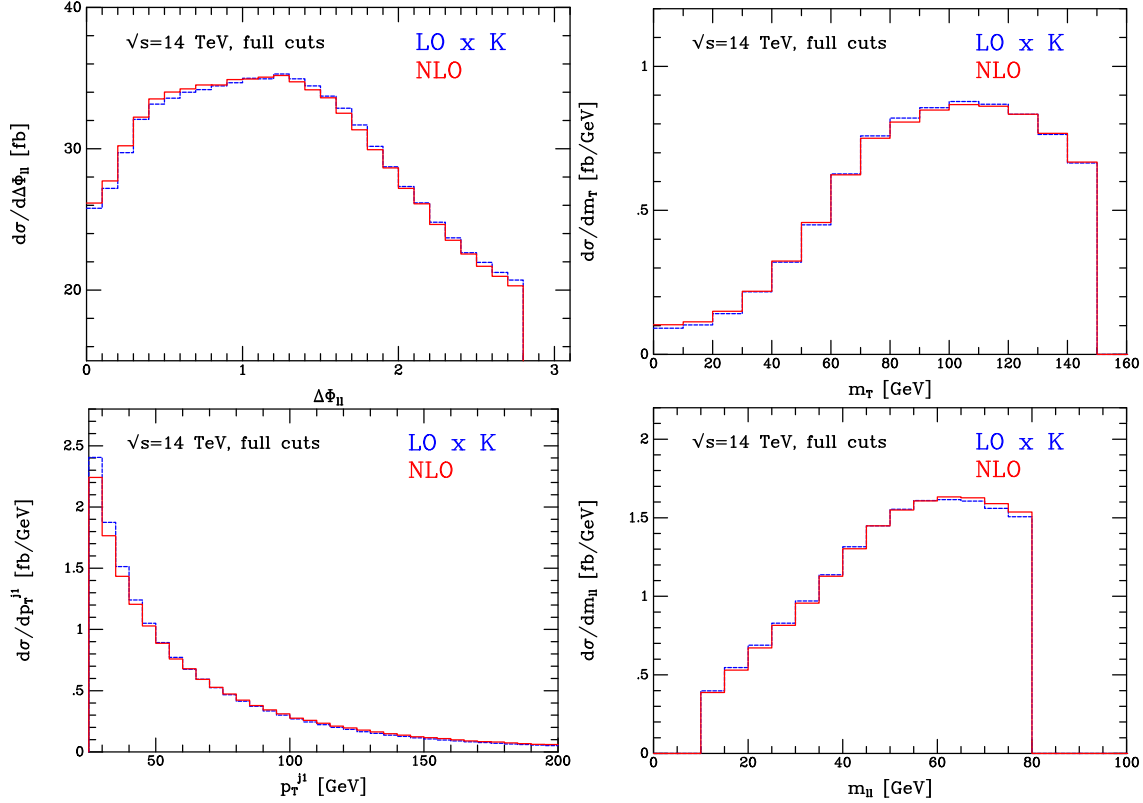


FIG. 5: Kinematic distributions at 14 TeV, using the full set of cuts specified in the text. The NLO prediction is shown as the solid (red) histogram, while the dashed (blue) histogram corresponds to the LO prediction rescaled by the  $K$ -factor from Table V.

variable	cut
$p_{\perp,j}$	$> 30$ GeV
$ \eta_j $	$< 4.5$
$ \eta_\ell $	$< 2.5$
$p_{\perp,\ell_1}$	$> 50$ GeV
$p_{\perp,\ell_2}$	$> 10$ GeV
$p_{\perp}^{\text{miss}}$	$> 20$ GeV
$m_T^{\ell\ell}$	$> 80$ GeV

TABLE VI: Cuts applied in the 100 TeV analysis, corresponding to the “full” set of cuts. The jet cuts, corresponding to the first two lines in the table, are the only ones applied for the “basic” cross-section.

between the shapes of the distributions at each order, with the exception of the transverse momentum of the leading jet. In contrast this does receive significant corrections, which is expected since additional radiation beyond a single jet is only present at NLO.

The corresponding distributions after the application of the spin-2 cuts, i.e. the addition of the transverse momentum cut in Eq. (15), are shown in Figure 6. The additional cut has little effect on the distributions, except for  $p_{\perp}^{j1}$ . This exhibits a discontinuity at 125 GeV, reflecting the fact that the NLO prediction is not reliable in this region due to the kinematic limitation present at LO ( $p_{\perp}^{j1} = p_{\perp}^H$ ).

For our 100 TeV analysis, we take as inspiration the CMS search for additional heavy resonances

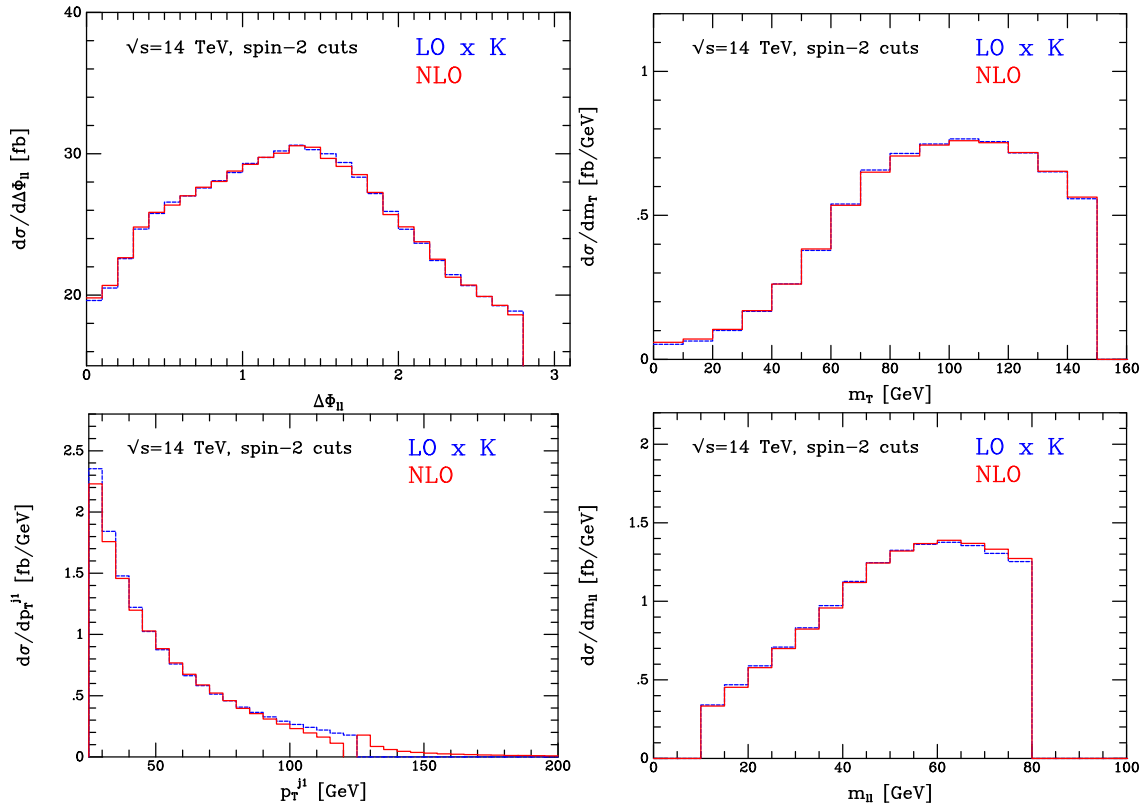


FIG. 6: Kinematic distributions at 14 TeV, using the spin-2 set of cuts specified in the text. The labelling is as in Figure 5.

presented in Ref. [11]. Such resonances can appear in models with extended Higgs sectors, where the simplest realization contains an additional scalar which is a singlet under all SM gauge groups [59, 60] (see also [61, 62] and references therein). This can be interpreted as a limiting case for more generic BSM scenarios, e.g. models with either additional gauge sectors [63] or matter content [64, 65]. In such models, the decay modes for the additional heavy scalar are dominated by  $WW$  decays with branching ratios of order 80% or higher [62]; therefore the process considered here constitutes a dominant SM background. Furthermore, as the parameter space of such models is severely constrained by electroweak precision measurements [66], direct production cross-sections at the LHC are typically of order a few tens of femtobarns, even for additional scalar masses below 1 TeV. Therefore, such models may be hard to constrain at the LHC and would remain to be investigated at a future 100 TeV proton-proton collider.

The cuts for our 100 TeV analysis are shown in Table VI, where we have adopted the  $p_{\perp}$  and  $m_T$  cut values used in searches for heavy resonances with masses greater than 200 GeV.<sup>2</sup> For the sake of simplicity we do not adopt the separation into strict jet bins performed in Ref. [11], nor do we discard two-jet events that fail the vector boson fusion selection cuts.<sup>3</sup> The cross-sections at 100 TeV are shown in Table VII. We again find that  $K$ -factors do not depend strongly on

<sup>2</sup> Note that in Ref. [11], the  $m_T^{\ell\ell}$  cut at 80 GeV in the case of heavy resonances is erroneously reported as a cut on  $E_{\perp, \text{miss}}$ . We thank X. Janssen for clarifying this point.

<sup>3</sup> The vector boson fusion selection cuts correspond to  $m_{jj} > 500$  GeV and  $\Delta\eta_{jj} > 3.5$  [11]. In our case such cuts can only apply to real radiation contributions that are present at NLO. We find that these amount to about 90 fb, which can be used as an order of magnitude estimate of contamination for the pure VBF-type signal from quark-induced  $WW + 2$  jets at leading order.

cuts	$\sigma^{\text{LO}}$ [pb]	$\sigma^{\text{NLO}}$ [pb]	$K$
basic	6.815(1)	7.939(5)	1.16
full	1.237(1)	1.471(1)	1.19

TABLE VII: cross-sections at 100 TeV, for the cuts specified in Table VI. Monte Carlo uncertainties are indicated in parentheses and are smaller than the per mille level.

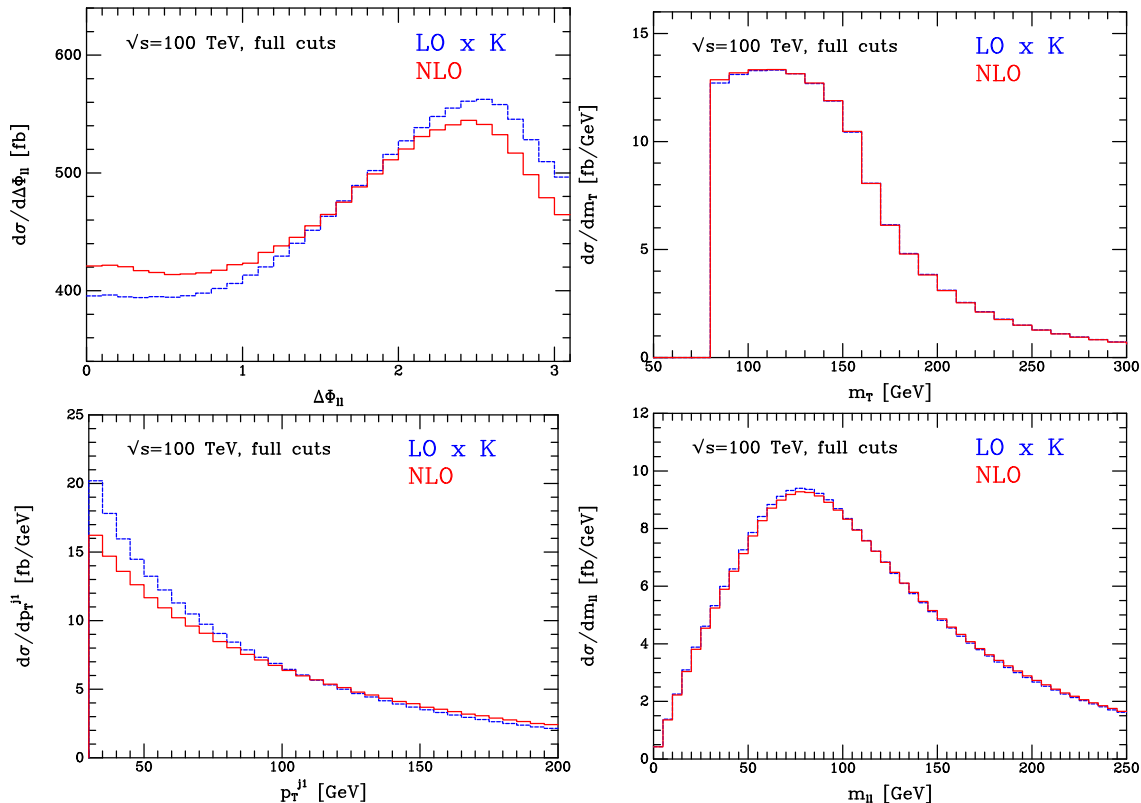


FIG. 7: Kinematic distributions at 100 TeV, using the full set of cuts specified in the text. The labelling is as in Figure 5.

the choice of cuts. In Figure 7 we again display differential distributions in our usual kinematic quantities,  $m_T^{\ell\ell}$ ,  $\Delta\Phi_{\ell\ell}$ ,  $m_{\ell\ell}$ , and  $p_{\perp}^{j1}$ , showing both NLO as well as rescaled LO results. We observe that a correct description of the  $\Delta\Phi_{\ell\ell}$  and  $p_{\perp}^{j1}$  distributions requires the inclusion of the full NLO corrections. On the other hand, the distributions for  $m_T^{\ell\ell}$  and  $m_{\ell\ell}$  are both well described using a rescaled LO calculation.

#### 4. CONCLUSIONS

In this paper we have presented a calculation of  $WW$  production in association with a jet at next-to-leading order in QCD using generalized unitarity methods. These methods allow the one-loop amplitude to be determined in a relatively compact analytic form. As examples, we have shown several expressions for the coefficients of box, triangle, and bubble scalar integrals that appear in the amplitudes. Our calculation has been implemented in the parton level Monte Carlo generator MCFM, which contains analytic expressions for the complete virtual amplitude. The

MCFM code is significantly faster than previous publicly available implementations of the one-loop amplitudes. To demonstrate the effect of including NLO corrections, we have studied several cases of phenomenological interest where the  $WW$ +jet process serves as an important background. These included studies of the CP properties and spin of the recently-discovered Higgs boson at the LHC, as well as searches for additional scalar resonances at a 100 TeV proton-proton collider. We have provided cross-section predictions for both scenarios, and examined a number of kinematic distributions relevant for the experimental analyses. For several of these, and especially the  $p_{\perp}$  distribution of the first jet, the fixed order NLO description is significantly different from the prediction obtained at LO.

Apart from the phenomenological studies, the full analytic expression for the virtual amplitude is an important ingredient in the determination of the  $WW$  production cross-section at next-to-next-to-leading order. These contributions will be made available in the release of the next version of the MCFM code.

### Acknowledgements

TR thanks Simon Badger, Ruth Britto, Fabrizio Caola, Pierpaolo Mastrolia, and Ciaran Williams for extremely useful discussions during this work, as well as the Fermilab theory group for their hospitality. DJM is supported by the UK Science and Technology Facilities Council (STFC) under grant ST/L000446/1. DJM and TR also want to thank A.A.H. Graham for contributions during the early stages of this work. This research is supported by the US DOE under contract DE-AC02-07CH11359.

- 
- [1] G. Aad et al. (ATLAS), Phys.Rev. **D87**, 112001 (2013), 1210.2979.
  - [2] Tech. Rep. ATLAS-CONF-2014-033, CERN, Geneva (2014), URL <http://cds.cern.ch/record/1728248>.
  - [3] S. Chatrchyan et al. (CMS Collaboration), Phys.Lett. **B721**, 190 (2013), 1301.4698.
  - [4] G. Aad et al. (ATLAS), JHEP **1501**, 049 (2015), 1410.7238.
  - [5] G. Aad et al. (ATLAS), Phys.Rev. **D91**, 052005 (2015), 1407.0573.
  - [6] Tech. Rep. CMS-PAS-SMP-14-016, CERN, Geneva (2015), URL <http://cds.cern.ch/record/2002016>.
  - [7] S. Chatrchyan et al. (CMS), Eur.Phys.J. **C73**, 2610 (2013), 1306.1126.
  - [8] S. Chatrchyan et al. (CMS), Phys.Lett. **B699**, 25 (2011), 1102.5429.
  - [9] S. Chatrchyan et al. (CMS), Eur.Phys.J. **C73**, 2283 (2013), 1210.7544.
  - [10] V. Khachatryan et al. (CMS), Phys. Rev. **D92**, 012004 (2015), 1411.3441.
  - [11] V. Khachatryan et al. (CMS) (2015), 1504.00936.
  - [12] Tech. Rep. ATLAS-CONF-2013-067, CERN, Geneva (2013), URL <https://cds.cern.ch/record/1562879>.
  - [13] G. Chachamis, M. Czakon, and D. Eiras, JHEP **0812**, 003 (2008), 0802.4028.
  - [14] G. Chachamis, M. Czakon, and D. Eiras (2008), 0806.3043.
  - [15] T. Gehrmann, M. Grazzini, S. Kallweit, P. Maierhofer, A. von Manteuffel, et al., Phys.Rev.Lett. **113**, 212001 (2014), 1408.5243.
  - [16] A. von Manteuffel and L. Tancredi, JHEP **06**, 197 (2015), 1503.08835.
  - [17] F. Caola, J. M. Henn, K. Melnikov, A. V. Smirnov, and V. A. Smirnov, JHEP **1506**, 129 (2015), 1503.08759.
  - [18] T. Gehrmann, A. von Manteuffel, and L. Tancredi (2015), 1503.04812.
  - [19] R. Boughezal, C. Focke, X. Liu, and F. Petriello (2015), 1504.02131.
  - [20] J. Gaunt, M. Stahlhofen, F. J. Tackmann, and J. R. Walsh (2015), 1505.04794.
  - [21] R. Britto, F. Cachazo, and B. Feng, Nucl.Phys. **B725**, 275 (2005), hep-th/0412103.

- [22] R. Britto, E. Buchbinder, F. Cachazo, and B. Feng, *Phys.Rev.* **D72**, 065012 (2005), hep-ph/0503132.
- [23] R. Britto, B. Feng, and P. Mastrolia, *Phys.Rev.* **D73**, 105004 (2006), hep-ph/0602178.
- [24] D. Forde, *Phys.Rev.* **D75**, 125019 (2007), 0704.1835.
- [25] P. Mastrolia, *Phys.Lett.* **B678**, 246 (2009), 0905.2909.
- [26] S. Badger, *JHEP* **0901**, 049 (2009), 0806.4600.
- [27] L. J. Dixon and Y. Sofianatos, *JHEP* **0908**, 058 (2009), 0906.0008.
- [28] S. Badger, E. Nigel Glover, P. Mastrolia, and C. Williams, *JHEP* **1001**, 036 (2010), 0909.4475.
- [29] S. Badger, J. M. Campbell, R. K. Ellis, and C. Williams, *JHEP* **0912**, 035 (2009), 0910.4481.
- [30] S. Badger, R. Sattler, and V. Yundin, *Phys.Rev.* **D83**, 074020 (2011), 1101.5947.
- [31] S. Badger, J. M. Campbell, and R. Ellis, *JHEP* **1103**, 027 (2011), 1011.6647.
- [32] J. M. Campbell and C. Williams, *Phys.Rev.* **D89**, 113001 (2014), 1403.2641.
- [33] T. Dennen and C. Williams, *Phys.Rev.* **D91**, 054012 (2015), 1411.3237.
- [34] R. Boughezal, F. Caola, K. Melnikov, F. Petriello, and M. Schulze, *JHEP* **1306**, 072 (2013), 1302.6216.
- [35] X. Chen, T. Gehrmann, E. Glover, and M. Jaquier, *Phys.Lett.* **B740**, 147 (2015), 1408.5325.
- [36] R. Boughezal, F. Caola, K. Melnikov, F. Petriello, and M. Schulze (2015), 1504.07922.
- [37] R. Boughezal, C. Focke, W. Giele, X. Liu, and F. Petriello, *Phys. Lett.* **B748**, 5 (2015), 1505.03893.
- [38] J. M. Campbell, R. K. Ellis, and G. Zanderighi, *JHEP* **0712**, 056 (2007), 0710.1832.
- [39] S. Dittmaier, S. Kallweit, and P. Uwer, *Phys.Rev.Lett.* **100**, 062003 (2008), 0710.1577.
- [40] G. Sanguinetti and S. Karg (2008), 0806.1394.
- [41] S. Dittmaier, S. Kallweit, and P. Uwer, *Nucl.Phys.* **B826**, 18 (2010), 0908.4124.
- [42] F. Cascioli, S. Hoche, F. Krauss, P. Maierhofer, S. Pozzorini, et al., *JHEP* **1401**, 046 (2014), 1309.0500.
- [43] T. Melia, K. Melnikov, R. Rontsch, M. Schulze, and G. Zanderighi, *JHEP* **1208**, 115 (2012), 1205.6987.
- [44] J. M. Campbell and R. K. Ellis, *Phys.Rev.* **D60**, 113006 (1999), hep-ph/9905386.
- [45] J. M. Campbell, R. K. Ellis, and W. T. Giele, *Eur.Phys.J.* **C75**, 246 (2015), 1503.06182.
- [46] L. J. Dixon, Z. Kunszt, and A. Signer, *Nucl.Phys.* **B531**, 3 (1998), hep-ph/9803250.
- [47] S. Catani and M. Seymour, *Nucl.Phys.* **B485**, 291 (1997), hep-ph/9605323.
- [48] Z. Bern, L. J. Dixon, and D. A. Kosower, *Nucl.Phys.* **B513**, 3 (1998), hep-ph/9708239.
- [49] D. Maitre and P. Mastrolia, *Comput.Phys.Commun.* **179**, 501 (2008), 0710.5559.
- [50] R. K. Ellis and G. Zanderighi, *JHEP* **0802**, 002 (2008), 0712.1851.
- [51] R. K. Ellis, W. T. Giele, Z. Kunszt, and K. Melnikov, *Nucl.Phys.* **B822**, 270 (2009), 0806.3467.
- [52] Z. Bern et al. (NLO Multileg Working Group), pp. 1–120 (2008), 0803.0494.
- [53] J. Alwall, M. Herquet, F. Maltoni, O. Mattelaer, and T. Stelzer, *JHEP* **1106**, 128 (2011), 1106.0522.
- [54] J. Alwall, R. Frederix, S. Frixione, V. Hirschi, F. Maltoni, et al., *JHEP* **1407**, 079 (2014), 1405.0301.
- [55] J. Pumplin, D. Stump, J. Huston, H. Lai, P. M. Nadolsky, et al., *JHEP* **0207**, 012 (2002), hep-ph/0201195.
- [56] H.-L. Lai, M. Guzzi, J. Huston, Z. Li, P. M. Nadolsky, et al., *Phys.Rev.* **D82**, 074024 (2010), 1007.2241.
- [57] C. Berger, Z. Bern, L. J. Dixon, F. Febres Cordero, D. Forde, et al., *Phys.Rev.* **D80**, 074036 (2009), 0907.1984.
- [58] G. Aad et al. (ATLAS), *Eur.Phys.J.* **C75**, 231 (2015), 1503.03643.
- [59] R. Schabinger and J. D. Wells, *Phys.Rev.* **D72**, 093007 (2005), hep-ph/0509209.
- [60] B. Patt and F. Wilczek (2006), hep-ph/0605188.
- [61] G. M. Pruna and T. Robens, *Phys.Rev.* **D88**, 115012 (2013), 1303.1150.
- [62] T. Robens and T. Stefaniak, *Eur.Phys.J.* **C75**, 104 (2015), 1501.02234.
- [63] L. Basso, S. Moretti, and G. M. Pruna, *Phys.Rev.* **D82**, 055018 (2010), 1004.3039.
- [64] M. J. Strassler and K. M. Zurek, *Phys.Lett.* **B651**, 374 (2007), hep-ph/0604261.
- [65] M. J. Strassler and K. M. Zurek, *Phys.Lett.* **B661**, 263 (2008), hep-ph/0605193.
- [66] D. Lopez-Val and T. Robens, *Phys.Rev.* **D90**, 114018 (2014), 1406.1043.